Advances in Science and Technology Research Journal

Advances in Science and Technology Research Journal, 2027, 21(1), 557–577
https://doi.org/10.12913/22998624/237429
ISSN 2299-8624, License CC-BY 4.0

Received: 2026.09.14
Accepted: 2026.11.15
Published: 2026.12.01

Non-local structural consequences of a localized fire beneath a continuous prestressed concrete box girder

Viet-Hung Tran[1], Thai-Son Vu[1], Thi-Nguyet-Hang Nguyen[1*]

[1] Department of Bridge and Road Engineering, Hanoi University of Civil Engineering, 55 Giai Phong Street, Bach Mai Ward, Hanoi 11618, Vietnam
* Corresponding author's e-mail: hangntn@huce.edu.vn

ABSTRACT

Structural fire assessment is organized around the heated member, an organization that is exact only for statically determinate elements. This numerical study examines the demand that a localized fire beneath the deck imposes on the unheated parts of a continuous prestressed concrete box-girder bridge of 35 + 50 + 35 m. Two-dimensional heat transfer with temperature-dependent properties is reduced to an equivalent axial thermal strain, a thermal curvature, and a degraded flexural stiffness imposed on the girder. The framework is verified against grid and time-step refinement, closed-form solutions, and a second, independent implementation; it has not been validated against experiments. For a 20 m hydrocarbon fire at midspan, the hogging moment at the never-heated intermediate support rises by 48.8% after 240 min, and restrained thermal curvature supplies 75% or 96% of that increase, depending on the order in which the two mechanisms are introduced. The support, 7% more utilized than midspan at ambient temperature, becomes 6.4 times as utilized, and a check confined to the fire-exposed member reports 60 to 67% of the system demand for the five fire positions compared. The ratio of the two checks factorizes exactly into the relative increase of the support moment, the ambient utilization balance of the competing sections, and the resistance retention of the heated one. The first factor is positive in every variant examined; the other two depend on the design, and cracked supports or a draped continuity tendon can bring the ratio to unity or below. Utilization ratios compare an elastic demand with an ultimate resistance and do not predict collapse.

Keywords: prestressed concrete, box-girder bridge, localized fire, statically indeterminate structure, restrained thermal curvature, moment redistribution, structural fire assessment.

INTRODUCTION

The space beneath urban viaducts and approach ramps is a scarce resource, commonly occupied by parking, storage, and small businesses. The resulting fire load sits immediately below the soffit of the superstructure, a hazard that was reviewed systematically enough to identify the principal gaps in its treatment [1]. A fire in a motorcycle park beneath an approach ramp of the Vinh Tuy Bridge in Hanoi in 2025 illustrates this exposure. The incident motivates the study; the idealized model analyzed below isolates the mechanics. No attempt is made to reconstruct the Vinh Tuy event, which would require bridge-specific geometry, a documented exposure history, and forensic data. Concrete structures in fire have been studied systematically at the material and member levels. The degradation of compressive strength and elastic modulus with temperature is well characterized [2, 3]. Explosive spalling driven by pore pressure has been described in comparable detail [4, 5]. Design procedures are codified in EN 1992-1-2 [6] and in ACI/TMS 216.1 [7]. A risk-based importance factor grades bridges by fire exposure [8]. A recent review documents the accident record for bridges of all types [9]; another treats the fire behavior of girders, prestressed and steel alike [10]. Numerical models of localized fires beneath a deck exist for steel girder bridges [11], one of which reproduces an actual fire-induced collapse [12].

Research in Vietnam is more recent and has concentrated on individual members. The shear resistance of prestressed hollow-core slabs in fire has been quantified experimentally and numerically [13, 14]. The ambient-temperature contribution of polypropylene and steel fibers to the web-shear resistance of the same member type has also been established [15]. The flexural performance of prestressed I-girders under a hydrocarbon fire has been examined [16], with the contribution of surface fire-protection materials [17]. Reinforcement layout and cover thickness in high-strength concrete beams have been analyzed with the 500 °C isotherm method [18].

Three levels of a single research gap emerge from this body of work. The first is locality: assessment is organized around the heated member or the heated section, an organization inherited from determinate elements, in which the thermal deformation develops freely, the temperature field produces only a self-equilibrated stress system, and, to first order, the internal forces due to the mechanical loading are unchanged. The second is structural redundancy: in a continuous bridge, the free thermal curvature is restrained by redundant supports, thereby generating additional internal forces that propagate well beyond the fire, while the local loss of flexural stiffness simultaneously redistributes the mechanical load effects towards the regions that retain their stiffness. Moment redistribution of this kind is well documented for continuous concrete members. It has been modeled for continuous reinforced concrete beams under a local fire [19] and measured on continuous T-beams tested to failure [20]; a sectional method that separates the effects of thermal deformation from those of the vertical load has been proposed for continuous beams under standard fire [21]; and the rotation capacity that such redistribution demands at heated intermediate supports has been modeled for statically indeterminate slabs and beams [22]. All four concern reinforced concrete beams and slabs at the member scale. The principles governing members whose thermal deformation is restrained, in particular the distinction between restrained expansion and restrained bowing, were formalized a quarter of a century ago [23]. The influence of restraint has since been quantified for concrete beams [24] and for unbonded post-tensioned slabs [25]. The third is governing-section migration: because both redundant effects increase the hogging moment over an intermediate support outside the fire zone, the critical section can move there, so that a local sectional check may report both the wrong utilization ratio and the wrong location. A comparable system-scale effect has been reported for a steel cable-stayed bridge, where a fire at one girder segment altered the internal force distribution of the whole bridge [26], and for continuous steel–concrete composite girders, the fire resistance of which depends strongly on whether the fire lies at midspan or over the hogging zone [27]. Prestressed concrete box girders have been analyzed under hydrocarbon fire with three-dimensional nonlinear finite-element models [28, 29] and tested in furnaces [30, 31]; these studies address the fire resistance of individual girders. The demand that a localized fire transfers to a never-heated support of a continuous concrete box-girder bridge, and the share of that demand attributable to each redundant mechanism, have not been quantified directly. The box cross-section adds a geometric feature to this sequence: in the hogging region around an intermediate support, the bottom slab is the compression zone, so a fire beneath the deck heats the compression zone directly, the opposite of a simply supported girder, in which the heated face is the tension zone and the dominant concern is the tendon temperature.

EN 1992-1-2 [6] already draws the distinction on which the first of these levels rests: it separates member analysis, analysis of parts of the structure, as well as global structural analysis, and permits indirect fire actions to be neglected only in the first. What it does not supply is the size of the deficit that follows from performing the first where the third is required, the location to which the governing section then moves, or the proportion in which the two redundant mechanisms contribute. These three quantities are established below, and the local assessment used for comparison is the member analysis that the code itself permits.

Unlike the member-scale studies of continuous concrete beams [19–22], the present study addresses a multi-span box-girder bridge under a localized hydrocarbon fire. Unlike the three-dimensional models and furnace tests of box girders [28–31], it treats the girder as a redundant system and resolves the demand outside the heated length. The contribution is mechanistic: the study identifies, separates and quantifies the two mechanisms by which a localized thermal action produces non-local demand, and derives an exact factorization of the error of a member-level check. The reduced-order formulation is complementary to experimentally validated three-dimensional

models. It gives up local failure modes such as spalling, shear, and tendon anchorage in exchange for the ability to isolate the redundant mechanisms and to evaluate several hundred configurations. Three objectives follow: to construct a two-step framework determining the temperature field in a box cross-section and reducing it to an equivalent sectional deformation; to separate the additional bending moment into a restrained-thermal-deformation and a stiffness-degradation contribution, and to express their proportion as a mechanism ratio traced against fire duration and fire-zone length; to define a compact diagnostic, the non-local amplification factor, measuring the error of the conventional local check, to identify the parameters that control it, and to establish how far the migration of the governing section survives changes in the model. Figure 1 summarizes the causal chain these objectives address.

MATERIALS AND METHODS

Heat transfer in the cross-section

In this subsection and the two that follow, the pair (x, y) denotes a position within the cross-section, x is transverse and y is upward from the soffit; from Eq. (10) onwards, x is the longitudinal coordinate along the bridge. The temperature field $\theta(x, y, t)$ over the cross-section is obtained from the non-linear two-dimensional heat conduction equation

$$\rho_c(\theta)\, c_p(\theta)\, \partial\theta/\partial t = \nabla \cdot [\lambda_c(\theta)\, \nabla\theta] \qquad (1)$$

in which the density ρ_c, the specific heat c_p, and the thermal conductivity λ_c are temperature dependent and taken from EN 1992-1-2 [6], using the lower conductivity limit recommended there for concrete structures and the specific-heat curve for a moisture content of 1.5% by weight, whose peak between 100 and 200 °C represents evaporation of free water. On a fire-exposed boundary, the net heat flux combines convection and radiation,

$$\dot{h}_{net} = \alpha_c(\theta_g - \theta_s) + \Phi\, \varepsilon_m\, \varepsilon_f\, \sigma\, [(\theta_g + 273)^4 - (\theta_s + 273)^4] \qquad (2)$$

where: $\dot{h}_{net}$ is the net heat flux per unit area, θ_g and θ_s are the gas and surface temperatures in °C, σ is the Stefan–Boltzmann constant, the product of the surface and fire emissivities is $\varepsilon_m\, \varepsilon_f = 0.7$, and the configuration factor is $\Phi = 1$.

Equation (2) uses the implementation's absolute-temperature offset of 273 K against the 273.15 K of EN 1991-1-2, of negligible effect here. The convective coefficient α_c is 25 W/(m²·K) for the standard curve and 50 W/(m²·K) for the hydrocarbon curve [32]; on the unexposed boundaries (the top of the deck and the internal faces of the cell void), a combined coefficient of 9 W/(m²·K) towards 20 °C applies. Radiative exchange between the internal faces of the closed cell is not modeled; after 240 min, the internal faces of the webs remain below 44 °C, and the upper face of the bottom slab reaches about 60 °C, so its effect

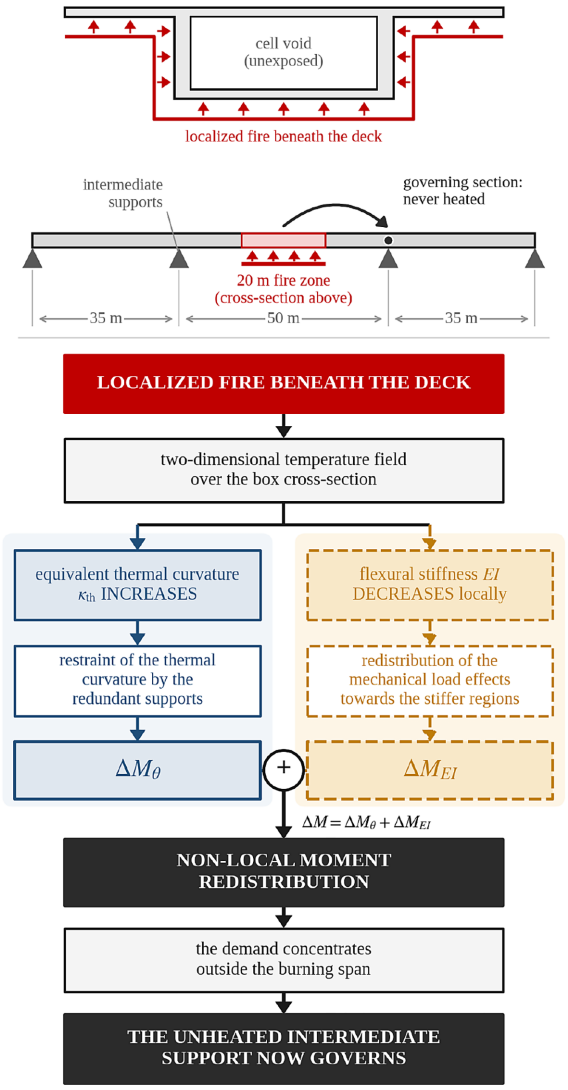


Figure 1. Causal chain of the non-local redistribution mechanism: a localized fire produces a two-dimensional temperature field which simultaneously raises the equivalent thermal curvature and lowers the flexural stiffness of the heated length; restraint of the first and redistribution of the second generate the two additive moment contributions whose sum concentrates the demand at an unheated intermediate support

on the deck slab and its tendons is small. The tendons and ducts are not discretized as separate materials, and the temperature of each tendon is interpolated from the concrete field at its axis. The two temperature–time curves of EN 1991-1-2 are

$$\theta_g = 20 + 345 \log_{10}(8t + 1) \tag{3}$$

$$\theta_g = 20 + 1080 \left(1 - 0.325\, e^{-0.167t} - 0.675\, e^{-2.5t}\right) \tag{4}$$

with t in minutes. A vehicle fire beneath a bridge involves petrol and polymeric materials and develops faster than a cellulosic fire, so Eq. (4) is the reference scenario and Eq. (3) is retained for comparison [32]. Purpose-derived parametric curves for under-deck tanker fires have since been proposed for I-girder bridges [33], and the hydrocarbon curve has been adopted as the reference exposure in previous analyses of prestressed concrete box girders [28].

Temperature-dependent material properties

The free thermal strain of siliceous aggregate concrete follows EN 1992-1-2,

$$\varepsilon_{th}(\theta) = \min(-1.8 \times 10^{-4} + 9 \times 10^{-6}\,\theta + 2.3 \times 10^{-11}\,\theta^3,\ 14 \times 10^{-3}) \tag{5}$$

Equation (5) is the cubic branch of the code model, valid for $20 \le \theta \le 700$°C, the ceiling applying above 700°C. A temperature-dependent stiffness reduction factor is built from the secant stiffness to peak stress of the Eurocode stress–strain relation and normalized to the ambient elastic modulus $E_c(20)$, using the strength reduction factor $k_c(\theta)$ and the strain at peak stress $\varepsilon_{c1}(\theta)$,

$$E_c(\theta)/E_c(20) = k_c(\theta)\, \varepsilon_{c1}(20)/\varepsilon_{c1}(\theta) \tag{6}$$

Equation (6), therefore, gives the temperature reduction of the effective flexural stiffness; it does not imply that $E_c(20)$ is itself the secant modulus at peak stress. Because the stress–strain curve flattens as temperature rises, stiffness degrades faster than strength [34, 35]. The strength reduction factor of the prestressing steel, $k_p(\theta)$, is taken from EN 1992-1-2 for cold-worked steel of class A.

Equivalent sectional thermal deformation

Assuming plane sections, $\varepsilon(y) = \bar{\varepsilon} + \kappa(y - y_E)$ with y measured upwards from the soffit, the modulus-weighted centroid and the sectional stiffnesses are

$$EA = \int_A E_c\, dA,\ y_E = (1/EA) \int_A E_c\, y\, dA,$$
$$EI = \int_A E_c\, (y - y_E)^2\, dA \tag{7}$$

Requiring that no axial force and no moment act on a free section, with the sectional stiffnesses of Eq. (7), gives the equivalent axial thermal strain and thermal curvature,

$$\bar{\varepsilon}_{th} = (1/EA) \int_A E_c\, \varepsilon_{th}\, dA,\ \kappa_{th} = (1/EI) \int_A E_c\, \varepsilon_{th}\, (y - y_E)\, dA \tag{8}$$

while the residual self-equilibrated stress produced by the nonlinear part of the temperature field is

$$\sigma_{res}(y) = E_c(\theta)\, [\bar{\varepsilon}_{th} + \kappa_{th}\, (y - y_E) - \varepsilon_{th}(\theta)] \tag{9}$$

For a determinate member, Eq. (9) is the complete mechanical consequence of the fire at the sectional level; for an indeterminate system, $\bar{\varepsilon}_{th}$ and κ_{th} become eigen-deformations imposed on the structure and generate additional internal forces. That difference is the origin of every non-local effect reported below. The reduction assumes plane sections and a temperature field that is uniform along the fire zone, so that longitudinal conduction and the transition at the ends of the fire zone are not represented. Within those assumptions, it loses no information that the beam model can use. Equation (8) is the unique pair $(\bar{\varepsilon}_{th}, \kappa_{th})$ that leaves the residual stress of Eq. (9) without axial force or moment, and the spatial detail discarded by the beam model is carried entirely by that self-equilibrated residual. The vertical asymmetry of the field enters through κ_{th} and through the upward shift of y_E. The transverse variation enters through the weights $E_c(\theta)$ and the lever arms of Eq. (8), and for the transversely symmetric exposure considered here, the thermal curvature about the vertical axis vanishes identically.

Additional internal forces and the mechanism ratio

For an Euler–Bernoulli beam with the vertical displacement w positive upwards, the stress-free state of an element inside the fire zone corresponds to a curvature $\chi = -\kappa_{th}$, the sign following because the strain parameter κ of Eq. (8) is the negative of the displacement curvature w'' under the convention adopted here, and the energy functional is

$$U = \tfrac{1}{2} \int_0^L EI(x)\, [w'' - \chi]^2\, dx - \int_0^L q\, w\, dx \tag{10}$$

in which L is the length of the girder. The transverse load q is a signed intensity, positive in the

+w direction, so the downward gravity load of the accidental combination enters as $q = -p_{fi}$. Stationarity of Eq. (10), discretized with two-node Hermite elements, gives the element load vector $\boldsymbol{f}_{\chi} = EI\,\chi\,\{0\ -1\ 0\ 1\}^{T}$ and the bending moment

$$M(x) = EI(x)\,[w''(x) - \chi(x)] \tag{11}$$

The Euler–Bernoulli idealization rests on the slenderness of the girder: the span-to-depth ratios are 14 and 20, and the shear parameter $EI_{20}/(GAL^2)$ of the center span is 0.0025, GA being the shear stiffness of the two webs over the full depth. Repeating the reference analysis with shear-flexible (Timoshenko) elements, with the web shear stiffness reduced over the fire zone in proportion to the integrated modulus, 0.628 of its ambient value after 240 min, changes the moment at the governing support by 0.4% for the fire at midspan and by 0.8% for the fire at x_c = 70 m, and the relative increase from 48.8 to 49.0%. For a fire centered at midspan the shear flexibility of the heated length does not enter, because the redundant moments are symmetric and the virtual shear force in the center span vanishes. The exposure and the load are symmetric about the vertical axis of the section, so they induce neither torsion nor cross-sectional distortion. Shear lag in the 12 m deck slab is not represented.

Equation (11) applies at element level, EI and χ being constant over each element at a given step, consistent with the piecewise-constant material update. Equation (12) below is a telescoping identity and holds for any intermediate state; what linearity at each instant supplies is the interpretation of its second term. The increase of the bending moment relative to the ambient state is written

$$\Delta M = \Delta M_{\theta} + \Delta M_{EI} \tag{12}$$

where: $\Delta M_{EI} = M(q, EI_{fi}, 0) - M(q, EI_{20}, 0)$ and $\Delta M_{\theta} = M(q, EI_{fi}, \kappa_{th}) - M(q, EI_{fi}, 0)$, where $M(q, EI, \kappa)$ is the bending moment under load q, stiffness distribution EI, and sectional thermal curvature κ, the last entering the solution as $\chi = -\kappa$.

Their sum reproduces $M(q, EI_{fi}, \kappa_{th}) - M(q, EI_{20}, 0)$, and linearity makes ΔM_{θ} equal to $M(0, EI_{fi}, \kappa_{th})$, the response of the already-degraded structure to the thermal eigen-deformation alone. The intermediate state is a convention: ΔM_{EI} is evaluated first, at zero imposed curvature, and ΔM_{θ} is the increment added to the degraded stiffness, the physical sequence, the heated length being already softened as the curvature accumulates. The complementary ordering, the curvature imposed at EI_{20}, and the stiffness reduced afterward, telescopes to the same ΔM but returns R_{θ} = 0.964 rather than 0.752 at 240 min, because the thermal fixed-end moment scales with the stiffness of the element carrying it. The dominance of restrained thermal deformation does not depend on the choice; the precise share does. R_{θ} is therefore a state-decomposition metric attached to a stated ordering; it does not measure a unique physical fraction of the response. For two factors, an ordering-independent value exists, the mean of the two orderings, which is 0.858 at 240 min. The physical ordering is used below, and the complementary one is quoted where the distinction matters. R_{θ} is a share only when ΔM_{θ} and ΔM_{EI} have the same sign. This holds in the duration and length sweeps of Figure 7 and for fire centers at 60 and 70 m. When the fire covers a pier, the loss of stiffness at the support reduces its hogging moment, ΔM_{EI} changes sign, and R_{θ} exceeds unity, 1.22 at x_c = 77.5 m and 1.41 at 85 m, the whole increase then coming from restrained thermal curvature. The proportion in which they act is the dimensionless mechanism ratio

$$R_{\theta} = \Delta M_{\theta} / (\Delta M_{\theta} + \Delta M_{EI}),\ R_{EI} = 1 - R_{\theta} \tag{13}$$

evaluated at the intermediate support. The mechanism ratios are defined only where $\Delta M \neq 0$, so the histories below begin at the first non-zero snapshot, t = 5 min. Being an identity, Eq. (12) makes R_{θ} and R_{EI} sum to unity, and $R_{\theta} > 0.5$ states that restrained thermal deformation, not the degradation of stiffness in the heated length, dominates the additional demand. The bearings are assumed to permit longitudinal movement, so that $\bar{\varepsilon}_{th}$ generates no appreciable axial force, an assumption examined in the Discussion.

Flexural resistance, utilization ratio, and the non-local amplification factor

The flexural resistance is evaluated on the two-dimensional temperature field, not through an equivalent section. The tendon force is $F_p = A_p\,\bar{k}_p\,f_{pd}$, with A_p the tendon area of the region considered (Table 1) and $\bar{k}_p$ the mean strength reduction factor from bilinear interpolation of the field at the tendon level; the depth of the compression zone follows from equilibrium,

$$\int_{Ac} k_c(\theta)\,f_{cd}\,\mathrm{d}A = F_p \tag{14}$$

where: A_c is the compressed area measured from the extreme compression fiber, the resisting moment being the product of F_p and the lever arm between the tendon centroid and that of the compressive stress block.

Equation (14) is a simplified ultimate stress-block equilibrium: the steel reaches its temperature-reduced design strength, while prestress strain compatibility and the temperature-induced losses driven by thermal creep and relaxation of the prestressing steel [36] are not modeled. The limit state represented by $M_{Rd,fi}$ is therefore the ultimate flexural resistance of the section at elevated temperature. In the reference analysis, the prestressing force enters only through this resistance. No longitudinal tendon profile is specified, so the secondary moment a draped continuity profile generates in a continuous girder is not carried as an action: the moments below are load-effect moments, not complete design moments. It is itself an indeterminate effect of the same flexibility the fire degrades, so it would redistribute with the stiffness and add a third term to Eq. (12); its magnitude and sign follow from the profile adopted, and they are evaluated for one representative profile in the Discussion. Under a hogging moment, the extreme compression fiber is the underside of the bottom slab, the heated face. The safety of a section is expressed by the utilization ratio

$$u(x, t) = |M(x, t)| / M_{Rd,fi}(x, t) \qquad (15)$$

where: $M_{Rd,fi}$ is the sagging or hogging resistance, selected by the sign of M, and takes its ambient value outside the fire zone; the two are written $M^{+}_{Rd,fi}$ and $M^{-}_{Rd,fi}$ where both are tabulated.

Two assessments are compared throughout. In the *local* assessment (the procedure normally applied to determinate members), the fire-reduced resistances are checked against the internal forces of the ambient analysis, and the maximum of Eq. (15) is taken over the heated length only, as conventional practice interrogates the fire-exposed member and not the structure around it. In the *system* assessment, the internal forces are recomputed with the degraded stiffness and the imposed curvature of Eq. (8) in place, and the maximum is taken over the whole girder. Their ratio,

$$A_{NL} = u_{max,system} / u_{max,local} \qquad (16)$$

is termed the non-local amplification factor. It is a diagnostic, not a material or geometric property: $A_{NL} > 1$ measures what a local check misses and $A_{NL} < 1$ marks a conservative local check; $A_{NL} = 1$ does not imply that the demand is local, because Eq. (17) below can return unity with a large increase of the support moment. Being a ratio of two utilization ratios on the same structure at the same instant, it cancels errors common to both resistances but not those that differ: where the two checks nominate different sections, as at the fire-center positions x_c = 60.0 and 70.0 m, it carries the full ratio of the heated sagging to the unheated hogging resistance, and a 10% reduction of $M^{+}_{Rd,fi}$ would move it from 1.49 to 1.34. It is undefined where the local check returns a zero utilization ratio and ill-conditioned as that ratio approaches zero, so it is meaningful only where the fire zone carries appreciable ambient demand.

Bridge, fire scenario, and loading

The structure analyzed is a three-span continuous prestressed concrete box-girder bridge of 35 + 50 + 35 m with a single-cell cross-section of constant depth (Table 1 and Figure 2a), a common configuration for urban overpasses; the flexural response of large-span prestressed box girders of this type is routinely established by finite-element simulation at ambient temperature [37], the ambient counterpart of the analysis here. The cross-section is idealized deliberately: a single cell, constant depth, vertical webs, no haunches or local thickenings, which isolates the mechanism and should preserve it qualitatively while affecting its magnitude, because the two terms of Eq. (12) depend only on the redundancy and on the position of the heated concrete relative to the centroid.

The fire scenario is shown in Figure 2b. A fire of length L_f, centered at x_c, heats the underside of the bottom slab and of the two cantilevers, the outer faces of the webs, and the outer edges of the deck slab; the cell void and the top of the deck remain unexposed. The fire length L_f = 20 m, 0.4 of the center span, is a reference configuration chosen for the parametric study; it is not a code-defined dimension and is not claimed to be critical, and L_f is varied from 5 to 50 m below. Within the fire zone, the exposure is uniform in space and follows the hydrocarbon curve in time, a severe bounding exposure that does not reproduce the growth, decay, and spatial non-uniformity of an actual vehicle fire [38, 39]. The load corresponds to the accidental design situation of EN 1990 [40], with the permanent actions at their characteristic

Table 1. Geometry, material properties, and loading of the bridge analyzed

Parameter	Value	Parameter	Value
Span arrangement (m)	35 + 50 + 35	Concrete	C40/50, siliceous
Girder depth (mm)	2,500	Design strength f_{cd} (MPa)	26.7
Deck slab width (mm)	12,000	Elastic modulus $E_c(20)$ (GPa)	34.0
Bottom slab width (mm)	6,000	Tendons, f_{pd} (MPa)	1,617
Deck slab thickness (mm)	250	Tendon area, sagging region (mm²)	12,000
Bottom slab thickness (mm)	250	Tendon area, hogging region (mm²)	18,000
Web thickness (mm)	2 × 450	Tendon axis distance (mm)	150
Sectional area (m²)	6.30	Load in fire, p_{fi} (kN/m)	207
Flexural stiffness EI_{20} (GN·m²)	199.5	Initial moisture content (%)	1.5

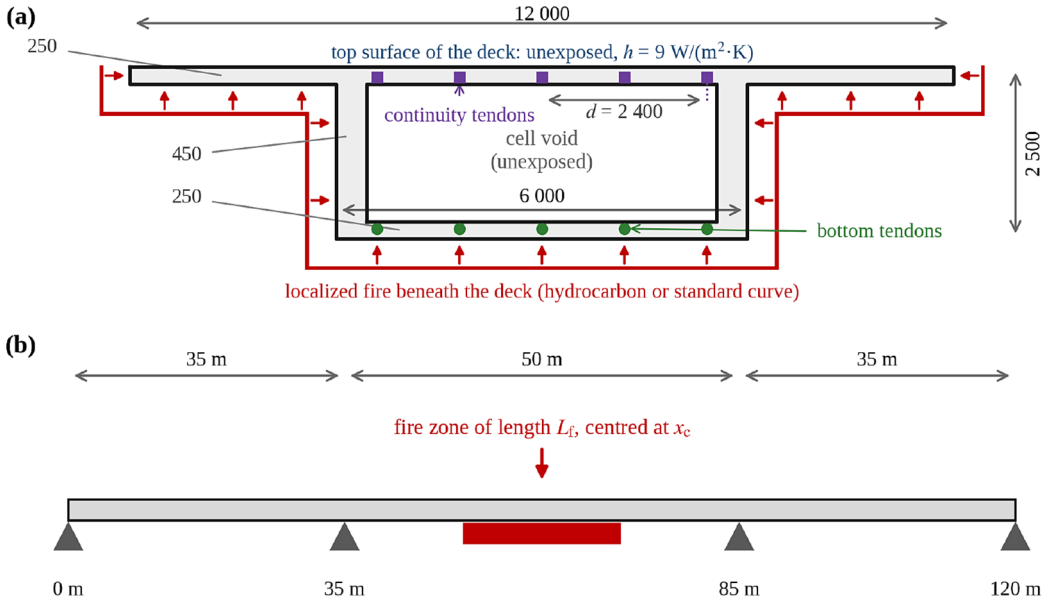


Figure 2. Object of the study: (a) box cross-section and thermal boundary conditions, dimensions in mm; (b) span arrangement and localized fire scenario. The tendon layout in (a) is schematic and corresponds to the baseline transverse spread, which is varied parametrically below

values and the traffic load taken as $\psi_{1,1}$ times the uniformly distributed load of Load Model 1 of EN 1991-2 [41] over the carriageway, which gives p_{fi} = 207 kN/m: 157.5 kN/m self-weight, 29.5 kN/m surfacing and parapets, and 20 kN/m traffic. The load is held constant throughout the fire. At ambient temperature the utilization ratio is 0.600 at the intermediate support and 0.560 at the center of the middle span.

Numerical implementation

Equation (1) is solved by an explicit, cell-centered finite-volume discretization on a uniform square grid of spacing Δx = 12.5 mm with a time step of 3 s. Every cross-sectional dimension is an integer multiple of that spacing, so the geometry is exact; any other grid distorts the slab and web thicknesses with no obvious symptom. The girder is discretized into 480 beam elements of 0.25 m.

The fire-exposed boundary is treated by resolving the surface temperature, rather than identifying it with the first cell center. That center is not on the surface, and evaluating Eq. (2), there would omit the half-cell conduction resistance $\Delta x/(2\lambda_c)$, under the hydrocarbon curve about five times the surface resistance, displacing the near-surface field deeper by roughly half a grid spacing. The surface temperature θ_s is therefore an unknown, obtained at every exposed cell and time step from flux continuity, $\alpha_c(\theta_g - \theta_s) + \Phi\, \varepsilon_m\, \varepsilon_f\, \sigma\, [(\theta_g + 273)^4 - (\theta_s + 273)^4] = (2\lambda_c/\Delta x)(\theta_s - \theta_{cell})$, by a vectorized Newton iteration on θ_s, the half-cell conductivity taken at the mean

of θ_s and the first-cell temperature θ_{cell}; it needs at most 10 passes to an increment below 10^{-7} K, with a largest flux residual of 2.9×10^{-6} W/m². On unexposed faces, this reduces to the series conductance $1/(1/h + \Delta x/(2\lambda_c))$, h being the combined unexposed-face coefficient of 9 W/(m²·K), and every quantity read at a depth is interpolated on a profile including the resolved surface node. Because that conductance is bounded by $2\lambda_c/\Delta x$ however severe the fire, the stability limit rises to about 63 s, so the adopted step of 3 s is 0.047 of it.

Five checks were carried out. Halving the grid spacing to 6.25 mm changes *EI* at 120 min by 0.08%, the thermal curvature by 0.05% and the hogging resistance by 0.01%; over all sectional quantities and times the sensitivity lies within 0.0–1.5% and is no longer one-signed, the half-cell offset having been eliminated: refinement deepens the 500 °C isotherm by 0.004 mm at 60 min and 0.079 mm at 120 min and makes it 0.072 mm shallower at 240 min, while the two spacings, the independent solution and the one-dimensional reference agree to within 0.21% at 60, 120 and 240 min. Halving the time step to 1.5 s changes every quantity of Table 2 by at most 0.04 % at 60, 120, 180 and 240 min, and the utilization ratio at the support by less than 10^{-5}. The residual stress field of Eq. (9) is self-equilibrated to within 2.4×10^{-8} N and 3.3×10^{-8} N·m over the 49 snapshots, referred to *EA* and *EI*, a spurious strain of 1.1×10^{-19} and curvature of 1.6×10^{-19} m^{-1}, that is, round-off. Three closed-form solutions are reproduced to within 0.0017%: a simply supported beam under uniform load, the same beam under an imposed uniform curvature, for which the moment must vanish, and a two-span beam under it. The 500°C isotherm in the bottom slab under the standard curve is 20.7 mm at 60 min and 36.0 mm at 120 min, against 21.5 mm from Annex A of EN 1992-1-2 for a 300 × 600 mm beam heated on three sides at 60 min [6], a difference of 3.8% within the spread attributable to geometry and exposure. Both use the 12.5 mm grid adopted throughout. Utilization ratios are quoted to three decimal places because the two implementations agree at that level; the spread produced by the modeling assumptions (Table 7) is much larger.

Independent verification by a second implementation

The framework has been re-implemented in a second, purpose-written code that shares no routine with the implementation above and uses a different numerical method at each step. No commercial or third-party finite-element package is involved. This is verification against an independent implementation of the same mathematical model, not experimental validation, so it does not test any physical assumptions listed in the Discussion.

Equation (1) is solved by a Galerkin finite-element formulation with linear triangular elements on a graded mesh of 13,536 nodes and 26,280 elements, refined from 157 mm in the deck slab to 0.30 mm at the fire-exposed faces, so the exposed surface is itself a line of nodes, and integrated by a fully implicit backward Euler step of 5 s with Picard iteration on the temperature-dependent properties to 10^{-3} K and a row-sum lumped capacity matrix, which keeps the scheme monotone across the steep front; a one-dimensional finite-volume model of the bottom slab at 0.25–1 mm supplies a third reference near the surface.

The girder is analyzed by the force method, not the displacement method: the two intermediate support moments are the redundant unknowns, and the flexibility coefficients follow from unit-load integrals of $w'' = M(x)/EI(x) + \chi(x)$ by composite 10-point Gauss–Legendre quadrature on sub-intervals respecting every discontinuity of *EI* and of χ, so the piecewise variation is integrated exactly without displacement interpolation. This independent implementation returns the exact three-span ambient value of 39.4888 MN·m, and its independently transcribed EN 1992-1-2 property laws agree with the primary code to machine precision.

The two implementations agree closely. Every ambient quantity agrees to within 0.01%. After 240 min of hydrocarbon fire the exposed-soffit temperature differs by 0.004%, the mean tendon-level temperature by 0.14% and the 500 °C isotherm depth by 0.04%, and the sectional and structural quantities by 0.50% on the axial thermal strain, 0.38% on the curvature, 0.21% on the residual stiffness ratio, 0.10% on the support hogging moment and 0.19% on the midspan deflection. The principal result, the increase of the hogging moment, is 48.8% against 49.0%, its separation according to Eq. (13) is 75.2 / 24.8% in both, and the utilization ratio at the unheated support is 0.894 against 0.895. The largest difference over all quantities is 1.01%, in the residual midspan sagging moment (the small difference of two large quantities), and over all temperatures, 0.74%, of the same order as the independent model's own discretization error, about 0.5%, so the comparison cannot resolve below that level.

RESULTS

Temperature field and equivalent thermal deformation

Figure 3 shows the temperature field after 240 min of hydrocarbon fire. The exposed surface approaches the gas temperature within minutes, but the gradient is steep: the 500 °C isotherm reaches only 29.1 mm into the bottom slab at 60 min and 60.8 mm at 240 min, so the tendons at an axis distance of 150 mm reach 150°C, a strength reduction factor of 0.935.

Figure 4a shows a pronounced transverse variation within the deck slab: the part above the cell void is essentially unheated, whereas the cantilever, exposed from below, reaches 297 °C after 240 min at the continuity-tendon level, interpolated there rather than read from the nearest cell. Figure 4b compares the computed 500 °C isotherm depth with the code benchmark. Therefore, the cell void insulates the central deck slab, while the cantilever is the vulnerable component, a distinction lost when a box section is reduced to a one-dimensional profile.

The equivalent axial strain and thermal curvature increase monotonically and show no saturation within 240 min, the heat continuing to penetrate deeper (Figure 5a). After 240 min, $\bar{\varepsilon}_{th}$ = 598 × 10^{-6} and $|\kappa_{th}|$ = 342 × 10^{-6} m^{-1}. The standard curve gives smaller values, but not in proportion: the curvature is 8% smaller and the axial strain only 5% smaller, because the curvature weights the hottest concrete, furthest from the centroid, more heavily. The sign of the curvature corresponds to bowing towards the heat source, as in the classical description of members heated on one face [23, 42].

Figure 5b summarizes the degradation of the three basic sectional quantities, tabulated at 60-minute intervals in Table 2. The flexural stiffness falls fastest, to 0.492 of its initial value after 240 min, because the heated concrete lies furthest from the modulus-weighted centroid and the modulus degrades faster than the strength, Eq. (6). The sagging resistance retains 0.935, its loss governed by the temperature of the bottom tendons behind the 250 mm slab. The hogging resistance retains 0.975, a small reduction noteworthy because the fire-exposed face forms the compression zone; repeating the calculation with the tendons held at 20 °C returns the same value, so the whole 2.5% loss belongs to that zone. It is small because the compressive force balancing the tendons occupies only the lower bottom slab, where enough cool concrete remains, and the lever arm is almost unaffected. Heating of the compression zone is therefore not the governing mechanism;

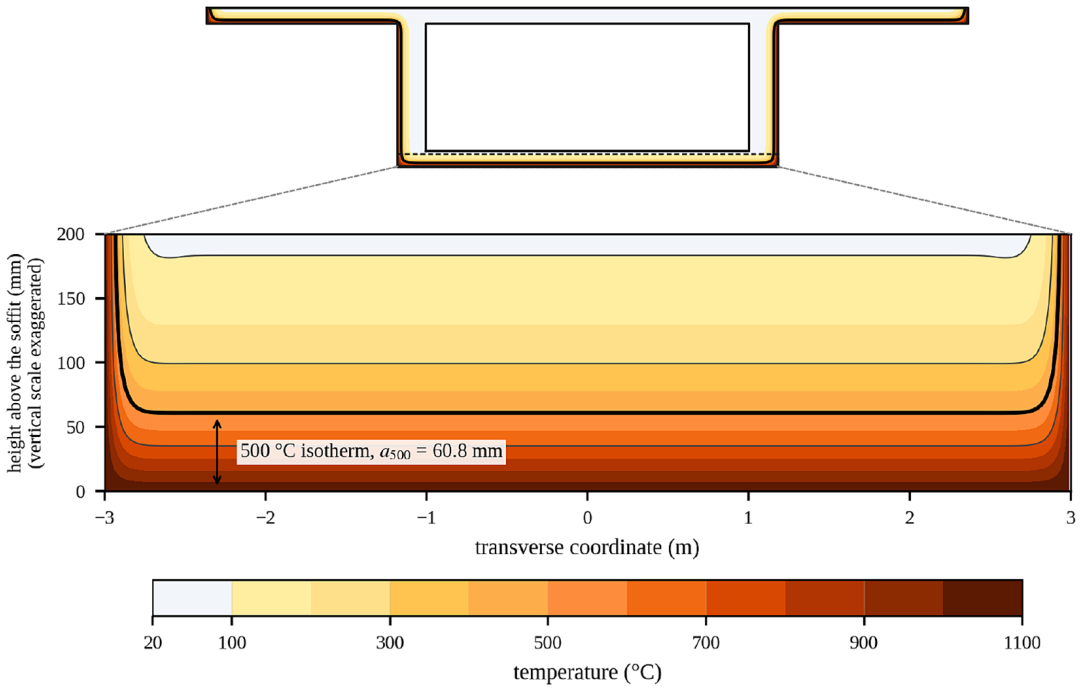


Figure 3. Temperature field in the box cross-section after 240 min of hydrocarbon fire, with the 500 °C isotherm highlighted and the lowest 200 mm of the bottom slab magnified

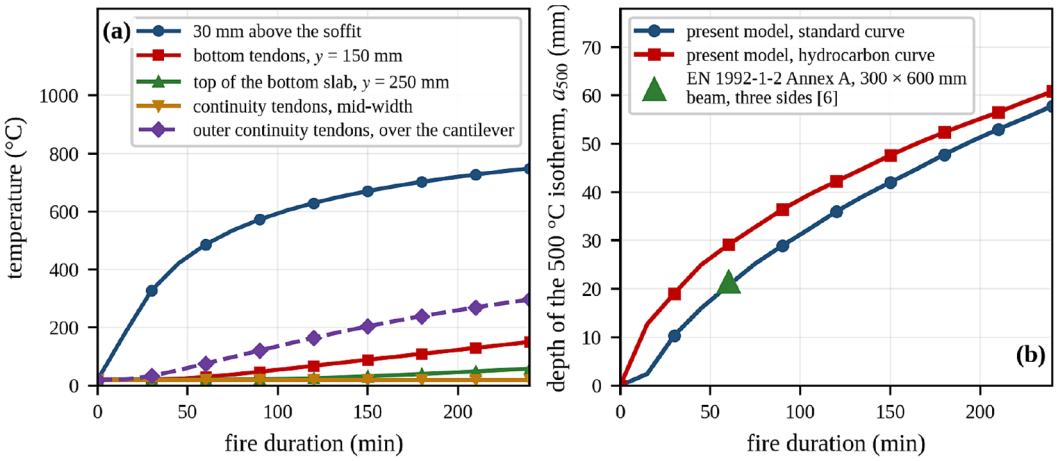


Figure 4. Thermal response and code comparison: (a) temperatures at characteristic points of the cross-section; (b) depth of the 500 °C isotherm compared with the value of Annex A of EN 1992-1-2 [6]

the transverse tendon position is. One-sided heating also drives the modulus-weighted centroid upwards, from 1.518 to 1.708 m, the eccentricity that generates the thermal curvature in Eq. (8).

Partitioning the numerator of the curvature in Eq. (8) by component after 240 min shows how the box geometry enters it. The bottom slab contributes 130% of the net thermal moment, the webs 27%, whereas the cantilevers, heated from below but lying above y_E, contribute −55% and the deck slab over the cell −3%. Had the cantilevers remained at ambient temperature, κ_{th} would be 534×10^{-6} m^{-1}, 1.56 times the computed value, so a representation that ignored the heating of the cantilevers would overstate the imposed curvature by 56%.

Table 2. Sectional response as a function of the duration of the hydrocarbon fire, tendon temperatures being mean values over the five tendon positions

t (min)	θ, bottom tendons (°C)	θ, top tendons (°C)	$\bar{\varepsilon}_{th}$ (10^{-6})	$\lvert\kappa_{th}\rvert$ (10^{-6} m^{-1})	EI_{fi}/EI_{20} (–)	$M^{+}_{Rd,fi}$ (MN·m)	$M^{-}_{Rd,fi}$ (MN·m)
0	20	20	0	0	1.000	45.02	65.76
60	30	20	236	104	0.740	45.02	64.95
120	68	20	373	180	0.630	45.02	64.59
180	110	20	494	260	0.551	44.46	64.32
240	150	20	598	342	0.492	42.11	64.10

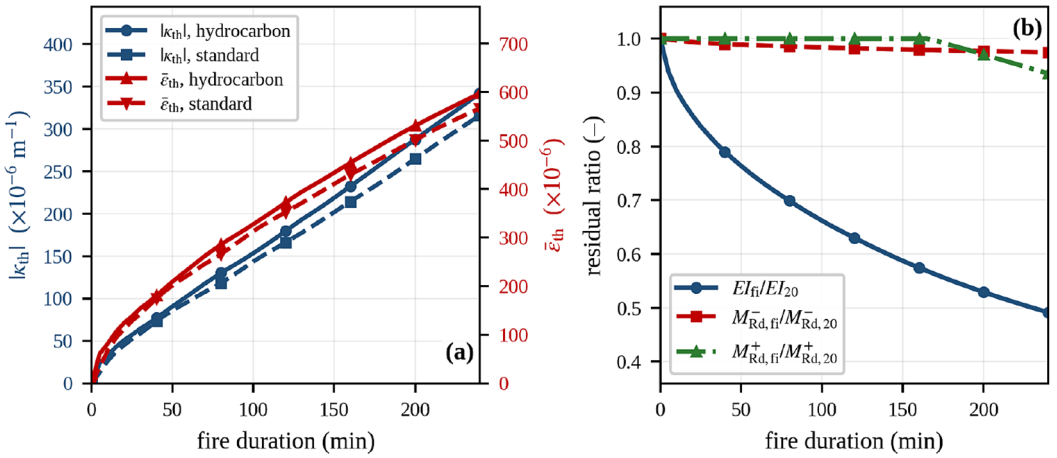


Figure 5. Sectional response under the hydrocarbon curve: (a) equivalent axial thermal strain and equivalent thermal curvature; (b) degradation of the flexural stiffness and of the sagging and hogging resistances

Non-local redistribution of internal forces

Figure 6a presents the bending moment diagram for a 20 m fire at the center of the middle span. The hogging moment at the two intermediate supports grows steadily with time while the sagging moment at midspan falls by the same amount: after 240 min the hogging moment at the support has risen from 39.49 to 58.77 MN·m, by 48.8%, and the sagging moment at midspan has fallen from 25.20 to 5.91 MN·m, a reduction of 76.5%.

The support section lies 15.0 m from the edge of the fire zone and is not heated: its resistance is unchanged, and the entire increase follows from the redundancy of the system rather than from any change in that section.

Therefore, the remaining safety margin concentrates on an undamaged section. At ambient temperature, the two are almost equally utilized, 0.600 against 0.560 at midspan, the support governing by some 7%; after 240 min midspan has fallen to 0.140 and the support risen to 0.894, so the ratio grows from about 1.07 to about 6.4, and the governing section is one that has never been heated.

Table 3 isolates the cause of this shift. The additional moment is the same, 19.28 MN·m, at the support and at midspan, because the redundant moment is uniform along the center span; it adds to the hogging moment at the support and subtracts from the sagging moment at midspan. With the fire-reduced resistances replaced by their ambient values, the support is 6.8 times as utilized as midspan, so the shift is carried by the action side of Eq. (15). Removing the thermal curvature leaves a ratio of 1.39, and removing the stiffness loss leaves 5.63. Restrained thermal curvature is therefore the primary cause, and stiffness degradation a secondary one, and continuity converts both into demand at a section the temperature, stiffness, and resistance of which do not change. Because the support already governs by 7% at ambient temperature in this configuration, the fire does not change which section of the system governs. It changes the margin between the two sections from 7% to a factor of 6.4, and it separates the section nominated by a check confined to the fire-exposed member from the section that governs the system. Where the heated span governs at ambient temperature, as in several variants of the Discussion, the fire moves the governing section to the support.

Separation of the two mechanisms

Figure 6b separates the increase according to Eq. (12). After 240 min, the restrained thermal deformation contributes 14.50 MN·m and the loss of stiffness 4.78 MN·m, so that R_θ = 0.752 and, for the ordering of Eq. (12), 24.8% of the additional demand originates in the loss of stiffness of the heated length. The distinction matters: at 60 min, the flexural stiffness has already fallen to 0.740 of its ambient value while the sagging and hogging resistances still retain 1.000 and 0.988 of theirs, because the modulus ratio of Eq. (6) falls to 0.625 at 100°C, where k_c is still 1.000; ΔM_{EI} measures a loss of stiffness, not of resistance. As

Table 3. Competing sections after 240 min of hydrocarbon fire, 20 m fire zone at x_c = 60.0 m. The support lies 15.0 m outside the fire zone and midspan at its center. Moments are magnitudes; *u* from Eq. (15); each of the last three rows changes one ingredient

Quantity	Intermediate support, *x* = 35 m	Midspan, *x* = 60 m
Tendon temperature (°C)	20	150 (bottom tendons)
$\lvert\kappa_{th}\rvert$ (10^{-6} m^{-1})	0	342
EI/EI_{20} (–)	1.000	0.492
Resistance M_{Rd} (MN·m)	65.76, hogging, ambient	42.11, sagging, fire-reduced
Moment, ambient (MN·m)	39.49	25.20
Additional moment (MN·m), ΔM_θ 14.50 and ΔM_{EI} 4.78	+19.28, more hogging	−19.28, less sagging
Moment after 240 min (MN·m)	58.77	5.91
u, ambient	0.600	0.560
u, full model	0.894	0.140
u, resistances held at ambient values	0.894	0.131
u, stiffness loss only (κ_{th} = 0)	0.673	0.485
u, thermal curvature only ($EI = EI_{20}$)	0.883	0.157

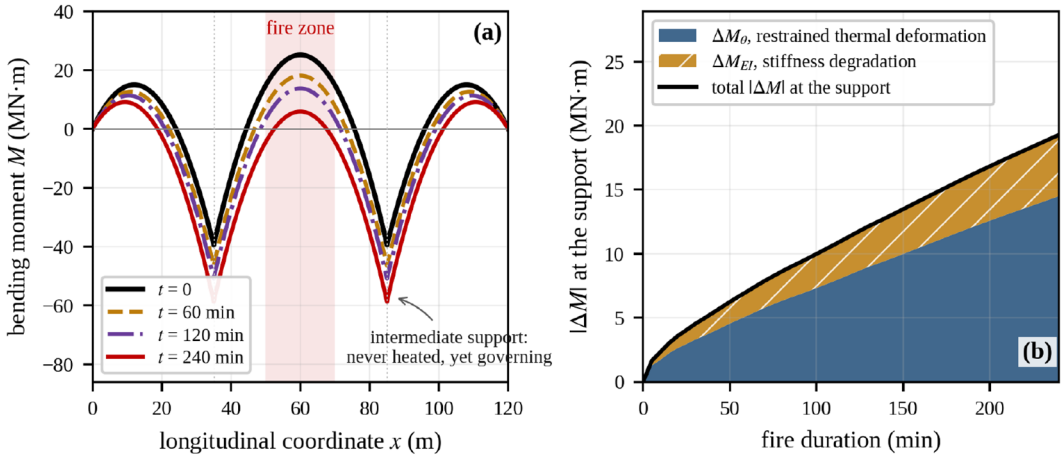


Figure 6. Structural response of the continuous girder: (a) bending moment diagram for a 20 m fire at the center of the middle span; (b) separation of the two contributions to the increase of the hogging moment at the support

an identity, Eq. (12) has a residual of exactly zero; against a separate solve carrying the thermal load alone, the largest discrepancy over all snapshots is 6.4×10^{-11} MN·m.

Figure 7a follows R_θ from the first non-zero snapshot to 240 min; its evolution is neither monotonic nor wide-ranging. The ratio is highest at that snapshot, 0.773 at 5 min, falls to a minimum of 0.726 at about 35 min, and rises thereafter, monotonically from about 95 min, to 0.752 at 240 min, still below where it started. The early decline reflects the stiffness of the heated length which falls faster, relatively, than the thermal curvature accumulates while the surface is already hot and the section is still cold. What matters more than the shape is the narrow band: R_θ stays between 0.726 and 0.773, a spread of only 0.047, and is within 1% of its final value from about 180 min. The dominance of restrained thermal deformation is essentially constant: the restraint term is between 2.65 and 3.40 times the stiffness term at every instant, with no crossover for the stiffness of Eq. (6). The standard curve gives $R_\theta = 0.750$ at 240 min, so the proportion is insensitive to the two exposure curves examined. Figure 7b shows the dependence on the length of the fire zone after 240 min. R_θ increases monotonically with L_f, from 0.725 at $L_f = 5$ m through 0.752 at 20 m to 0.948 when the fire covers the whole middle span. The acceleration beyond about 20 m arises because ΔM_{EI} peaks near $L_f = 25$–30 m at 5.18 MN·m then falls to 1.50 MN·m (a stiffness loss uniform over a span produces almost no redistribution) while ΔM_θ keeps growing.

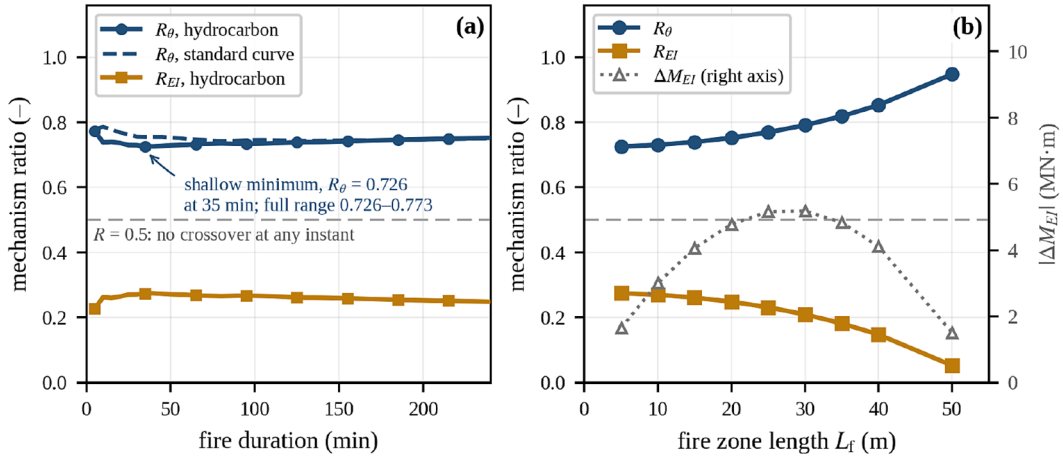


Figure 7. Separation of the two mechanisms: (a) mechanism ratios against fire duration for the reference fire, with the standard-curve result shown for comparison; (b) mechanism ratios against the length of the fire zone after 240 min, with the stiffness-degradation contribution on the right-hand axis

Local assessment against system assessment

Table 4 compares the two assessments defined by Eq. (16). The local procedure is non-conservative in every case: in the most severe scenario, it returns 0.598, which would be reported as satisfactory, against 0.999 from the system analysis. The two also disagree on the location of the governing section, wherever the fire zone does not reach an intermediate support: for x_c = 60.0 and 70.0 m the local check identifies midspan, whereas the governing section lies outside the fire zone. Once the fire covers the support, at x_c = 77.5 m and beyond, both nominate it, and the disagreement is one of magnitude alone.

That disagreement over location depends on how the local check is bounded. Extending it to every section, so that the unheated support is verified with its ambient resistance against its ambient moment, returns 0.600 instead of 0.598 at x_c = 60.0 m and nominates the support rather than midspan, a small margin, because the two sections begin the fire almost equally utilized, and 240 min lifts the heated midspan only to 0.598. Magnitude is unaffected: A_{NL} at x_c = 60.0 m is 1.49 on either bounding, and neither approaches the 0.894 of the system analysis.

For the five fire positions in Table 4, the non-local amplification factor after 240 min lies between 1.49 and 1.67, so the local procedure reports only 60 to 67% of the system-level demand-to-capacity measure. That range is a property of those five configurations. On a 0.5 m scan of 201 positions of the 20 m fire, counting only positions where the local check returns at least 0.5, it reaches 1.75 with the fire inside the center span and 1.88 with the fire in a side span; over the fire-length sweep it spans 1.16 at L_f = 5 m to 1.73 at L_f = 50 m, and it rises to 1.77 under the stiffer modulus definition bracketed in the Discussion. It becomes ill-conditioned as its denominator approaches zero: with the fire wholly inside a side span, x_c = 100 m, the denominator is 0.36, and the factor returns 2.72; that configuration is excluded above because there the local check interrogates a lightly loaded region rather than a differently damaged one.

A_{NL} also grows with fire duration in every configuration computed, rising for the reference fire from 1.26 at 60 min through 1.38 and 1.48 to 1.49 at 240 min without sign of saturation; as the duration approaches zero, it tends not to unity but to the ambient ratio 1.07, because the reference fire does not contain the section that governs at ambient temperature.

The structure of A_{NL} follows from Eqs. (15) and (16). Let s be the section that governs the system analysis and l the section nominated by the local check, $\delta = |M_{s,fi}|/|M_{s,20}| - 1$ the relative increase of the moment at s, $\rho_0 = u_{s,20}/u_{l,20}$ the ambient utilization ratio of the two sections, and r the retention factor of the resistance at l divided by that at s. Then:

$$A_{NL} = (1 + \delta)\, \rho_0\, r \tag{17}$$

is an algebraic identity whenever the moment at s keeps its sign, which is the case in all 211 configurations of the position and length sweeps. When the fire covers a pier, s and l coincide and A_{NL} = 1 + δ, between 1.51 and 1.60 for the 20 m fire. When the fire contains midspan, ρ_0 = 1.07 and r = 0.935, and A_{NL} lies between 1.49 and 1.67. When the fire lies inside the center span without reaching midspan, the local check interrogates less utilized sections, ρ_0 rises to 1.15 and A_{NL} to 1.75. The factor 1 + δ carries the mechanism, while ρ_0 and r are properties of the design and of the fire position. For the reference δ and r, a girder whose heated at ambient temperature with ρ_0 < 0.72 would make the local check conservative. The local check is bounded by the heated length. Whole-bridge bounding raises the two midspan entries to 0.600 and renames their governing section the intermediate support; every A_{NL} is then unchanged to two decimals except at x_c = 70.0 m, where it becomes 1.66.

Influence of the position and of the length of the fire zone

Figure 8a shows that the maximum utilization ratio depends strongly on the position of the fire, as sensitivity studies of steel bridges also find [43]. For a fire at the center of the middle span it reaches 0.894 after 240 min. As the fire moves towards the pier, the hogging moment grows further, and once the support falls inside the fire zone, its resistance decreases too. Over a scan of 201 positions at 0.5 m intervals, the most severe is x_c = 70.0 m, within 5 m of the pier, giving 0.999, a margin of the order of a tenth of a percent. In every position, the governing section is at an intermediate support, never in the burning span.

Figure 8b shows that the utilization ratio grows steadily with L_f but at a decreasing rate: the

Table 4. Local check compared with the system analysis after 240 min of hydrocarbon fire, for a 20 m fire zone

x_c (m)	u_{max}, local check (–)	Governing section, local check	u_{max}, system analysis (–)	Governing section, system analysis	A_{NL} (–)
60.0	0.598	Midspan	0.894	intermediate support	1.49
70.0	0.598	Midspan	0.999	intermediate support	1.67
77.5	0.616	Intermediate support	0.965	intermediate support	1.57
85.0	0.616	Intermediate support	0.930	intermediate support	1.51
92.5	0.616	Intermediate support	0.946	intermediate support	1.54

secant slope falls from 0.016 per meter between 5 and 10 m to 0.008 per meter between 20 and 30 m, because once the fire covers most of the span, extending it adds little to the accumulated imposed curvature. Unity is crossed at $L_f \approx 34$ m, by interpolation on a refined grid, only for a fire covering some 68% of the middle span, so the threshold demands a very extensive fire. Normalized by the center span L_2, the two parameters act differently. At midspan, over $0.1 \leq L_f/L_2 \leq 1.0$, the relative increase of the support moment grows from 0.15 to 0.73 and the maximum utilization ratio from 0.691 to 1.065. For $L_f/L_2 = 0.4$ and fire centers between the two piers, the relative increase stays between 0.49 and 0.66, and the maximum utilization ratio between 0.894 and 0.999. The length of the fire, therefore, controls the magnitude of the redistribution, while its position controls which pier governs and whether the member-level check nominates the correct section.

Influence of the fire curve and of the bottom-slab thickness

The hydrocarbon curve gives a maximum utilization ratio of 0.894 against 0.876 for the standard curve in the same configuration. The two converge to a similar gas temperature after a few hours, but over the first 60 min the hydrocarbon thermal curvature is 7.5% larger, so the choice of curve matters for short fire-resistance periods only.

Table 5 shows the effect of the bottom-slab thickness. Self-weight is adjusted for each variant, so the load rises as the slab thickens and the improvement is obtained despite the heavier section: increasing the thickness from 200 to 350 mm reduces the thermal curvature by 59% and, for a fire covering the intermediate support, the maximum utilization ratio from 0.962 to 0.834. The hogging resistance is practically unchanged across the four variants, because the ultimate compression block occupies only a shallow region adjacent to the soffit, so the additional bottom-slab material lies largely outside the compression zone; the benefit therefore comes almost entirely from the action side, a thicker slab reducing the eccentricity of the heated concrete and preserving a larger residual stiffness. This differs from cover in a solid beam, where the benefit lies mainly in keeping the reinforcement cooler [18].

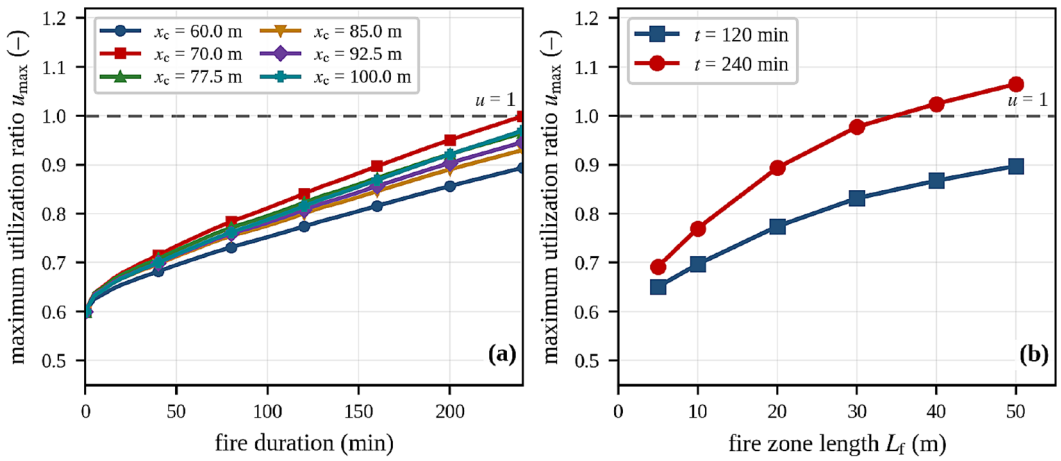


Figure 8. Maximum utilization ratio of the system: (a) influence of the position of the fire for a 20 m fire zone; (b) influence of the length of the fire zone for a fire at midspan

Table 5. Influence of the bottom-slab thickness after 240 min under the hydrocarbon curve, for a 20 m fire covering the intermediate support at x_c = 85.0 m and for the same fire at midspan at x_c = 60.0 m, the self-weight being adjusted to the sectional area of each variant

Bottom-slab thickness (mm)	p_{fi} (kN/m)	$\lvert\kappa_{th}\rvert$ (10^{-6} m^{-1})	EI_{fi}/EI_{20} (–)	$M^{-}_{Rd,fi}$ (MN·m)	u_{max}, fire at the support (–)	u_{max}, fire at midspan (–)
200	200.6	437	0.447	63.03	0.962	0.913
250	207.0	342	0.492	64.10	0.930	0.894
300	213.4	251	0.534	64.10	0.884	0.863
350	219.8	181	0.568	64.10	0.834	0.837

Transverse position of the continuity tendons

The transverse position of the hogging tendons was identified above as the quantity governing hogging resistance, and Table 6 confirms it; the parameter is the half-spread d of the outermost tendon group from the girder axis, the outer web face lying at 3.0 m. While the tendons lie inboard of the webs, the cell void keeps them near ambient (20 °C at d = 2.4 m after 240 min) and the hogging resistance retains 0.975, the small loss being the compression-zone effect above. Once they reach the outer web line, the cell void no longer shields them: at d = 3.0 m, the retained resistance falls to 0.921, and the maximum utilization ratio of the system rises from 0.965 to 1.022. Once they extend beyond it, they sit above the fire-exposed cantilever, their temperature rises to 297 °C, the retained resistance drops to 0.864, and the maximum utilization ratio rises to 1.088, an increase of 13% over the inboard arrangement. The change is concentrated at the web line, where the thermal boundary condition changes, and is complete within 0.6 m of it, the only parameter examined that steps rather than trends. Therefore, keeping the continuity tendons within the cell is the most efficient of the measures examined, acting on the resistance at no additional material cost.

Across the 479 configurations computed under the modulus of Eq. (6), 56 reach or exceed unity, in three identifiable families. Continuity tendons over the fire-exposed cantilever are the most severe, the widest spread, giving the largest value in the study, 1.119, with the fire at x_c = 75 m; Table 6 reports x_c = 77.5 m, where the same spread gives 1.088. Fire zones of 34 m and longer form the second. The third is not visible in Table 5: the 200 mm bottom slab exceeds unity at 7 of the 21 positions scanned, with a worst value of 1.033, though not at the two positions reported in the table. The standard curve never reaches unity, its largest value being 0.976. The margin is lost through identifiable design choices and the extent of the fire, not through the occurrence of a fire.

DISCUSSION

Robustness of the non-local redistribution mechanism

Three assumptions directly influence the computed utilization ratios, and all three have been tested, not to bound an error, but to separate results that are properties of the mechanism from results that are properties of the model.

The first is the elastic, uncracked material model. The residual stresses of Eq. (9) reach

Table 6. Influence of the transverse position of the continuity tendons, for a 20 m fire covering the intermediate support, centered at x_c = 77.5 m and by symmetry equivalent to x_c = 42.5 m, after 240 min under the hydrocarbon curve

Half-spread d (m)	$M^{-}_{Rd,fi}$ (MN·m)	$M^{-}_{Rd,fi}/M^{-}_{Rd,20}$ (–)	u_{max} (–)
2.4	64.10	0.975	0.965
2.8	64.10	0.975	0.965
3.0	60.54	0.921	1.022
3.2	56.90	0.865	1.087
3.6	56.84	0.864	1.088
5.0	56.84	0.864	1.088

34.7 MPa in tension and 29.1 MPa in compression after 240 min, the tensile value an order of magnitude above the mean tensile strength of C40/50 concrete, so the section will crack and the computed field is an upper bound relaxed by cracking and transient thermal creep, a component large enough for the Eurocode 2 model to have been reformulated to carry it explicitly [35]. Reducing the flexural stiffness to 0.4 EI_{20} over ±5 m at each intermediate support changes the relative increase of the support moment only from 48.8% to 51.5%, while the absolute utilization ratio falls from 0.894 to 0.725 and the mechanism ratio moves from 0.752 to 0.689: softening the support region changes the absolute safety index by about one fifth and the relative redistribution by three percentage points, and the support still governs after the fire. In this variant, the supports are cracked before the fire as well: midspan then governs at ambient temperature, with $u = 0.738$ against 0.479, the fire moves the governing section to the support, ρ_0 of Eq. (17) falls to 0.65, and A_{NL} to 0.92, so the local check is conservative although it nominates the wrong section. Cracking produced by the fire itself is represented by two further variants with an uncracked ambient girder. Cracking of the supports during the fire, 0.4 EI_{20} over ±5 m, gives an increase of 20.8%, $u = 0.725$ at the support, and $A_{NL} = 1.21$; because the secant formulation is path independent, this figure includes an 8.0 MN·m relief of the gravity hogging moment that is not a thermal effect. Cracking of the heated length, EI_{fi} reduced by a further factor of 0.4, gives 51.3%, 0.908, and 1.52, and the two together give 32.2%, 0.794, and 1.33. In all four variants, an intermediate support governs after the fire; the magnitude of the redistribution and the sign of the local check error depend on where and when the concrete cracks.

The second is the comparison between elastic demand and ultimate resistance. A plastic-mechanism check on the middle span, with hinges at the supports and midspan, gives a collapse load of 355 kN/m at ambient temperature and 345 kN/m after 240 min against $p_{fi} = 207$ kN/m, a load factor of 1.67. Restraint moments of this kind are self-canceling in a collapse mechanism, so a ratio approaching or exceeding 1.0 marks the onset of the redistribution mechanism check permitted, not incipient collapse; the elastic analysis locates where it is demanded, and that is not the burning span. The check also presupposes that the hogging sections can develop and sustain the rotation demanded; that is not verified here, and a prestressed hogging section the compression zone of which lies in the heated bottom slab is where the presupposition is least secure. Before u reaches unity, concrete in the heated length has already cracked in tension under the residual stresses of Eq. (9), and the heated compression zone of a support inside the fire zone may crush; the utilization ratio does not describe either event.

The third is the definition of the modulus. Equation (6) is the secant stiffness of the Eurocode stress–strain curve normalized to $E_c(20)$, and the strain at peak stress on which it depends carries transient creep implicitly; the explicit reformulation of that model was introduced for this reason [35]. Repeating the analysis with $E_c(\theta)/E_c(20) = k_c(\theta)$, which removes transient creep from the modulus without returning it to the strain, gives $EI_{fi}/EI_{20} = 0.802$ and $|\kappa_{th}| = 567 \times 10^{-6}$ m^{-1} after 240 min; the hogging moment at the support then rises by 76.6% rather than 48.8%, R_θ becomes 0.955 and the utilization ratio at the unheated support becomes 1.061, with the intermediate cases in Table 8. The two definitions span the range that the modulus assumption alone opens, without locating the answer inside it, and neither is complete: removing transient creep from the modulus without returning it to the strain overstates the stiffness, whereas retaining it inside $\varepsilon_{c1}(\theta)$ transfers a calibration obtained under sustained uniaxial compression to a different load path. Nor is the heated concrete lightly stressed (the field of Eq. (9) reaches a median 0.72 of the local reduced strength through the bottom slab), so the sign of the bias cannot be settled here, and the two endpoints bound the absolute utilization ratios rather than correcting them.

Cracking of the supports and the definition of the modulus act in opposite directions. The first softens the structure near the supports and reduces the restraint moment, the second stiffens the heated length and increases it; together, they give a utilization ratio at the support of 0.823. One distinction follows, and should govern how these results are used. Absolute utilization ratios are model-dependent, responding to the cracking assumption, the modulus definition, the resistance idealization of Eq. (14), and, at the level of a few percent, the discretization. The transfer of demand to the unheated support is more robust: it survives every combination examined and follows from the redundancy of the system. The magnitude of the relative redistribution is less robust; it ranges

from 21 to 77% across Table 7, and cracking of the supports during the fire is the variant that reduces it the most. The variations are deterministic one-at-a-time sensitivities with a few combined cases; no probability is attached to them, and they are not an uncertainty quantification. Table 7 collects them. In every variant, the hogging moment at the unheated support increases and, after 240 min, the maximum utilization lies at an intermediate support. The magnitude of that increase, the absolute utilization ratios, R_θ and A_{NL} are conditional on the modeling assumptions, and A_{NL} is also conditional on the design through ρ_0.

One code-supplied input has also been varied: the thermal conductivity, taken throughout at the lower of the two limits EN 1992-1-2 offers. With the upper limit the thermal step gives $|\kappa_{th}| = 451 \times 10^{-6}$ m^{-1}, a utilization ratio of 0.963 at the support and an increase of the support moment of 60.3%; the heat penetrates further, the 500°C isotherm reaching 63.8 mm and the bottom tendons 191°C, so $M^{+}_{Rd,fi}$ falls from 42.11 to 39.73 MN·m, the local check rises with it and A_{NL} reaches only 1.52. The surface boundary conditions were varied in the same way. Changing the resultant emissivity from 0.7 to 0.5 or 0.9, the convective coefficient of the hydrocarbon exposure from 50 to 25 W/(m²·K), or the coefficient of the unexposed faces from 9 to 4 W/(m²·K) changes κ_{th} after 240 min by at most 1.2% and u at the support by at most 0.003. After four hours of hydrocarbon exposure, the exposed surface is close to the gas temperature, so heat penetration is governed by the conductivity of the concrete, the only thermal input the code range of which changes the results materially.

Three consequences follow for practice. Reported post-fire assessments of concrete bridges have been organized around the visibly damaged region [44, 45], and cannot carry the assessment of a continuous bridge alone: the whole system

Table 7. Robustness of the reference case, 20 m hydrocarbon fire at x_c = 60.0 m after 240 min. Deterministic variants; 'governing' is the section of maximum u after the fire

Variant	Increase of support moment (%)	u at support (–)	Governing after fire	A_{NL} (–)
Reference	48.8	0.894	Intermediate support	1.49
Time step 1.5 s	48.8	0.894	Intermediate support	1.49
Shear-flexible elements	49.0	0.890	Intermediate support	1.48
Upper conductivity limit	60.3	0.963	Intermediate support	1.52
Resultant emissivity 0.5	48.7	0.893	Intermediate support	1.49
Resultant emissivity 0.9	48.9	0.894	Intermediate support	1.49
Convective coefficient 25 W/(m²·K)	48.8	0.893	Intermediate support	1.49
Unexposed-face coefficient 4 W/(m²·K)	49.3	0.896	Intermediate support	1.50
Supports cracked before and during fire	51.5	0.725	Intermediate support	0.92
Supports cracked during fire	20.8	0.725	Intermediate support	1.21
Heated length cracked, EI_{fi} × 0.4	51.3	0.908	Intermediate support	1.52
Supports and heated length cracked during fire	32.2	0.794	Intermediate support	1.33
Modulus $E_c(\theta)/E_c(20) = k_c(\theta)$	76.6	1.061	Intermediate support	1.77
Supports cracked before and during fire, modulus $k_c(\theta)$	72.0	0.823	Intermediate support	1.04
Secondary prestress, P = 9.9 MN	53.3	0.756	Intermediate support	1.47
Secondary prestress, P = 19.8 MN	60.2	0.619	Intermediate support	0.99
Secondary prestress, P = 24.8 MN	65.4	0.550	Intermediate support	0.81

Table 8. Sensitivity of the reference case to the definition of the modulus, after 240 min of hydrocarbon fire for a 20 m fire zone at $x_c = 60.0$ m. With $r = \varepsilon_{c1}(\theta)/\varepsilon_{c1}(20)$ the inflation of the strain at peak stress, the modulus ratio $E_c(\theta)/E_c(20)$ is set to $k_c(\theta)\, r^{-\beta}$, which retains a fraction β of that inflation geometrically: $\beta = 1$ recovers Eq. (6) and $\beta = 0$ gives $k_c(\theta)$. Each row recomputes the temperature field into $\bar{\varepsilon}_{th}$, κ_{th}, and EI_{fi} and re-solves the girder; the flexural resistances are unchanged across the rows, so the entire variation is on the action side

Modulus definition	EI_{fi}/EI_{20} (–)	$\lvert\kappa_{th}\rvert$ (10^{-6}m^{-1})	Support moment (MN·m)	Increase (%)	R_θ (–)	u at support (–)	A_{NL} (–)
$\beta = 1$, Eq. (6) as used above	0.492	342	58.77	48.8	0.752	0.894	1.49
$\beta = 0.75$	0.545	385	60.59	53.4	0.809	0.921	1.54
$\beta = 0.50$	0.611	437	62.97	59.5	0.863	0.958	1.60
$\beta = 0.25$	0.695	498	66.01	67.2	0.912	1.004	1.68
$\beta = 0$, $E_c(\theta)/E_c(20) = k_c(\theta)$	0.802	567	69.75	76.6	0.955	1.061	1.77

must be re-analyzed with the stiffness and imposed deformation updated to the temperature field, because the governing section may show no damage. Where that is impracticable, Eq. (17) indicates whether a member-level check is unconservative: A_{NL} exceeds unity when $(1 + \delta)\, \rho_0\, r > 1$, and ρ_0 and r follow from the ambient design. A_{NL} is a diagnostic for a given configuration; it is not a correction factor transferable between bridges. The two design parameters act on different terms of Eq. (15): a thicker bottom slab reduces the action ΔM_θ by reducing the eccentricity of the heated concrete, whereas keeping the continuity tendons inboard of the webs protects the resistance of Eq. (14) by using the cell void as a thermal shield: the more efficient, requiring no additional material. It is not, however, without cost: it concentrates 18,000 mm² of tendon within the central 5.1 m of a 12 m deck, with consequences for the transverse distribution of the hogging force, for shear lag, and for the anchorage layout, all outside the present scope.

Prestressing at elevated temperature

In the reference analysis, the prestressing system enters only through the resistance of Eq. (14), with the tendon temperature taken from the field. Two consequences of this simplification can be separated. On the resistance side, strain compatibility, relaxation, and thermal creep act only where the tendons are heated. At the unheated support, they change nothing, and at midspan a further loss of 84% of the fire-reduced sagging resistance would be required before the utilization ratio there reached that of the support after 240 min.

On the action side, a draped continuity tendon generates a secondary moment that redistributes with the stiffness and adds a third term to Eq. (12). It was evaluated for a representative parabolic profile, with the tendon axis 150 mm above the soffit at the low point of each span and 150 mm below the deck surface over the piers, and a force $P = 19.8$ MN, 18,000 mm² at 1,100 MPa, which balances 0.75 of the permanent load of the center span. The prestress enters the beam model as the eigen-curvature $-P\,e/EI$, e being the eccentricity of the tendon below y_E, the same device as Eq. (10), with EI, y_E, and P updated inside the fire zone. For consistency, the same 18,000 mm² tendon provides the sagging resistance at midspan, 67.09 MN·m at ambient temperature and 62.78 MN·m after 240 min. The secondary moment at the support, 14.1 MN·m sagging at ambient temperature, grows by 4.0 MN·m after 240 min because the heated length softens and its centroid rises. This offsets 21% of the 19.3 MN·m increase of Eq. (12), and 14, 8, and 1% when the tendon force in the heated length falls by 10, 20, and 30%. The relative increase in the support moment nevertheless rises to between 60 and 75%, because the ambient hogging moment is smaller.

The secondary moment also moves the ambient balance of the two sections. At $P = 19.8$ MN midspan governs at ambient temperature, with $u = 0.586$ against 0.386 at the support, and after 240 min, the support governs with u between 0.62 and 0.68 for the four tendon-force losses; the fire therefore moves the governing section, and A_{NL} lies between 0.99 and 1.08. For forces of 9.9, 19.8 and 24.8 MN and losses up to 30%, the support governs after the fire in every case, while A_{NL} ranges from 0.81 to 1.53 and follows ρ_0 of Eq. (17). The secondary moment leaves the transfer of demand to the unheated support in place; it changes the size, and possibly the sign, of the error of the member-level check.

Limitations and further work

The model has been verified numerically; it has not been validated against experiments, and no physical assumption listed here is tested by the verification. Five principal exclusions bound it, foremost among them cracking, examined only through the stiffness variants in Table 7 and without a cracked-section analysis; it has the largest effect on the magnitudes reported. Load-induced thermal strain is not modeled as a separate, explicit strain term: it enters implicitly through the strain at peak stress $\varepsilon_{c1}(\theta)$, so that Eq. (6) carries it in the stiffness while the free thermal strain of Eq. (5) does not, and Table 8 brackets the consequence of removing it. Temperature-induced prestress losses are excluded with Eq. (14); explosive spalling and the cooling phase are set out below. For C40/50 concrete at moderate moisture content, the spalling risk is lower than for high-strength concrete [4, 5]. In a fixed-temperature-field deletion sensitivity, removing the hottest and most expanded concrete (mean effective modulus only 0.019 of the ambient value) does not amplify the non-local mechanism: recomputing the sectional integrals with the lowest 15, 30 and 50 mm of the bottom slab absent (nominal depths on the 12.5 mm grid) gives $|\kappa_{th}|$ of 340, 334 and 303 × 10^{-6} m^{-1} and u at the support of 0.892, 0.889 and 0.869. Holding the field fixed never re-heats the fresh surface, whereas a real spall would expose cooler concrete to the fire, so the reductions are an upper bound. This is not a coupled spalling analysis: neither the timing of spalling nor the consequent tendon-temperature rise in the sagging region, where the governing section does not lie, is modeled. The bearings allow free longitudinal movement, so $\bar{\varepsilon}_{th}$ generates no appreciable axial force; a continuous deck slab or stiff frame piers would add restraint [23, 24]. The secondary prestress moment is absent from the reference analysis and evaluated above for one representative profile; a design-specific tendon layout would replace it. Shear lag in the deck slab is not represented. The fire zone is a rectangular footprint with uniform exposure, whereas a real fire decays in both directions; localized fire models for box-girder soffits [38] and traveling-fire representations [39] resolve that decay. During cooling, the heat penetrates deeper and the resistance falls further [46], so residual capacity needs a dedicated analysis [47]. The parametric study rests on the primary implementation alone, the independent comparison covering the reference scenario only. A continuous two-span specimen heated over part of one span, with the reaction at the unheated support measured, would test the mechanism directly; the furnace tests on prestressed concrete box girders [30, 31] are the natural starting point for such a test.

CONCLUSIONS

A localized fire beneath a continuous prestressed concrete box-girder bridge was analyzed as a non-local demand problem using a reduced-order framework that has been verified numerically but not validated experimentally. The findings hold within the investigated bridge configuration and fire scenarios. Within the investigated configuration, a localized fire transferred demand to an unheated intermediate support. For a 20 m hydrocarbon fire at midspan, the hogging moment there rose by 48.8% after 240 min while the section kept its temperature, stiffness, and resistance, and the margin between the support and the heated midspan grew from 7% to a factor of 6.4.

Restrained thermal curvature was the primary cause, and stiffness degradation was a secondary one. Their shares depend on the order in which they are introduced, 75% or 96% for the restraint term, and only the dominance of the restraint term is order-independent. The error of a member-level check factorizes exactly into the relative increase of the support moment, the ambient utilization balance of the competing sections, and the resistance retention of the heated one. For the reference girder and the five fire positions compared, the check reported 60 to 67% of the system demand. Supports cracked before the fire, or a secondary prestress moment from a draped continuity tendon, can bring it to unity or make it conservative. The transfer of demand to the unheated support survived every variant of the sensitivity study, whereas the absolute utilization ratios and the size of the underestimate did not. These results come from simulations. A continuous specimen heated over part of one span, with the reaction at the unheated support measured, is the experiment that would directly test the mechanism.

Acknowledgements

Financial support from Hanoi University of Civil Engineering under project number 12-2026/KHXD-TĐ is gratefully acknowledged. The authors declare no conflict of interest.

REFERENCES

1. Garlock M., Paya-Zaforteza I., Kodur V., Gu L. Fire hazard in bridges: Review, assessment and repair strategies. Eng. Struct. 2012; 35: 89–98. https://doi.org/10.1016/j.engstruct.2011.11.002
2. Kodur V.K.R., Wang T.C., Cheng F.P. Predicting the fire resistance behaviour of high strength concrete columns. Cem. Concr. Compos. 2004; 26(2): 141–153. https://doi.org/10.1016/S0958-9465(03)00089-1
3. Alaskar A. A comprehensive review on the influence of elevated temperatures on the mechanical performance of high-performance concretes. J. Umm Al-Qura Univ. Eng. Archit. 2025; 16(3): 879–890. https://doi.org/10.1007/s43995-025-00199-w
4. Phan L.T. Pore pressure and explosive spalling in concrete. Mater. Struct. 2008; 41(10): 1623–1632. https://doi.org/10.1617/s11527-008-9353-2
5. Amran M., Huang S.-S., Onaizi A.M., Murali G., Abdelgader H.S. Fire spalling behavior of high-strength concrete: A critical review. Constr. Build. Mater. 2022; 341: 127902. https://doi.org/10.1016/j.conbuildmat.2022.127902
6. EN 1992-1-2. Eurocode 2: Design of concrete structures, Part 1-2: General rules, structural fire design. Brussels: European Committee for Standardization; 2004.
7. ACI/TMS 216.1. Code requirements for determining fire resistance of concrete and masonry construction assemblies. Farmington Hills, MI: American Concrete Institute; 2014.
8. Kodur V.K.R., Naser M.Z. Importance factor for design of bridges against fire hazard. Eng. Struct. 2013; 54: 207–220. https://doi.org/10.1016/j.engstruct.2013.03.048
9. Gyawali S.S., Bhardwaj S.R., Anvari A.T., Aaleti S. Bridge fire accidents and research: A state-of-the-art review. Fire Technol. 2025; 61(7): 5319–5383. https://doi.org/10.1007/s10694-025-01787-x
10. Zhang G., Zhao X., Lu Z., Song C., Li X., Tang C. Review and discussion on fire behavior of bridge girders. J. Traffic Transp. Eng. (Engl. Ed.) 2022; 9(3): 422–446. https://doi.org/10.1016/j.jtte.2022.05.002
11. Paya-Zaforteza I., Garlock M.E.M. A numerical investigation on the fire response of a steel girder bridge. J. Constr. Steel Res. 2012; 75: 93–103. https://doi.org/10.1016/j.jcsr.2012.03.012
12. Alos-Moya J., Paya-Zaforteza I., Garlock M.E.M., Loma-Ossorio E., Schiffner D., Hospitaler A. Analysis of a bridge failure due to fire using computational fluid dynamics and finite element models. Eng. Struct. 2014; 68: 96–110. https://doi.org/10.1016/j.engstruct.2014.02.022
13. Nguyen T.-N.-H., Tan K.H. Shear response of deep precast/prestressed concrete hollow core slabs subjected to fire. Eng. Struct. 2021; 227: 111398. https://doi.org/10.1016/j.engstruct.2020.111398
14. Nguyen T.-N.-H., Li Y., Tan K.H. Shear behavior of fiber-reinforced concrete hollow-core slabs under elevated temperatures. Constr. Build. Mater. 2021; 275: 121362. https://doi.org/10.1016/j.conbuildmat.2020.121362
15. Nguyen T.-N.-H., Tan K.H., Kanda T. Effect of polypropylene and steel fibers on web-shear resistance of deep concrete hollow-core slabs. Eng. Struct. 2020; 210: 110273. https://doi.org/10.1016/j.engstruct.2020.110273
16. Tran V.-H., Phung B.-T., Vu D.-T., Nguyen T.-N.-H. Flexural performance of prestressed concrete I-shaped bridge girders exposed to hydrocarbon fire. J. Sci. Transp. Technol. 2025; 5(1): 61–76. https://doi.org/10.58845/jstt.utt.2025.en.5.1.61-76
17. Nguyen T.-N.-H. Effect of spray-applied insulating materials on flexural capacity of prestressed concrete slabs under fire conditions. J. Constr. 2025; 4/2025: 196–199. ISSN 2734-9888. (in Vietnamese)
18. Nguyen T.-N.-H., Tran V.-H. Flexural resistance of high-strength concrete beams in fire: Influence of key parameters based on the 500 °C isotherm method. J. Constr. 2026; 6/2026: 371–375. ISSN 2734-9888. (in Vietnamese)
19. Li Z., Ding F.-X., Cheng S. Numerical investigation on moment redistribution of continuous reinforced concrete beams under local fire conditions. Adv. Struct. Eng. 2021; 24(15): 3375–3388. https://doi.org/10.1177/13694332211026226
20. Xu Q., Han C., Wang Y.C., Li X., Chen L., Liu Q. Experimental and numerical investigations of fire resistance of continuous high strength steel reinforced concrete T-beams. Fire Saf. J. 2015; 78: 142–154. https://doi.org/10.1016/j.firesaf.2015.09.001
21. El-Fitiany S.F., Youssef M.A. Simplified method to analyze continuous reinforced concrete beams during fire exposure. ACI Struct. J. 2014; 111(1): 145–156. https://doi.org/10.14359/51686544
22. Bischof P., Morf U., Bamonte P., Kaufmann W. Modeling statically indeterminate reinforced concrete slabs and beams under fire conditions. Struct. Concr. 2023; 24(3): 3251–3263. https://doi.org/10.1002/suco.202200319
23. Usmani A.S., Rotter J.M., Lamont S., Sanad A.M., Gillie M. Fundamental principles of structural behaviour under thermal effects. Fire Saf. J. 2001; 36(8): 721–744. https://doi.org/10.1016/S0379-7112(01)00037-6
24. Dwaikat M.B., Kodur V.K.R. Response of restrained concrete beams under design fire exposure. J. Struct. Eng. 2009; 135(11): 1408–1417. https://

doi.org/10.1061/(ASCE)ST.1943-541X.0000058

25. Ellobody E., Bailey C.G. Modelling of unbonded post-tensioned concrete slabs under fire conditions. Fire Saf. J. 2009; 44(2): 159–167. https://doi.org/10.1016/j.firesaf.2008.05.007
26. Liu Z., Li G.-Q. Performance of steel cable-stayed bridges in ship fires, part I: Numerical method and baseline fire scenario study. J. Constr. Steel Res. 2023; 210: 108090. https://doi.org/10.1016/j.jcsr.2023.108090
27. Zhang G., Song C., Li X., He S., Huang Q. Fire performance of continuous steel-concrete composite bridge girders. KSCE J. Civ. Eng. 2021; 25(3): 973–984. https://doi.org/10.1007/s12205-021-0985-x
28. Song C., Zhang G., Hou W., He S. Performance of prestressed concrete box bridge girders under hydrocarbon fire exposure. Adv. Struct. Eng. 2020; 23(8): 1521–1533. https://doi.org/10.1177/1369433219898102
29. Zhang G., Kodur V., Xie J., He S., Hou W. Behavior of prestressed concrete box bridge girders under hydrocarbon fire condition. Procedia Eng. 2017; 210: 449–455. https://doi.org/10.1016/j.proeng.2017.11.100
30. Hou W., Zhang G., He S. Fire resistance tests on prestressed concrete box girder with intumescent fire-retardant coatings. Fire Technol. 2022; 58(1): 107–131. https://doi.org/10.1007/s10694-021-01145-7
31. Song C., Zhang G., Lu Z., Li X., Zhao X. Fire resistance tests on polypropylene-fiber-reinforced prestressed concrete box bridge girders. Eng. Struct. 2023; 282: 115800. https://doi.org/10.1016/j.engstruct.2023.115800
32. EN 1991-1-2. Eurocode 1: Actions on structures, Part 1-2: General actions, actions on structures exposed to fire. Brussels: European Committee for Standardization; 2002.
33. Howard J.D., Paya-Zaforteza I., Peris-Sayol G. Parametric fire curves for I-girder bridges submitted to under deck tanker fires. Eng. Struct. 2024; 306: 117810. https://doi.org/10.1016/j.engstruct.2024.117810
34. Fomin S., Butenko S., Plakhotnikova I., Koliesnikov S. Mathematical theory of stress-strain diagram for concrete under fire conditions and high temperatures. AIP Conf. Proc. 2023; 2684: 030011. https://doi.org/10.1063/5.0121302
35. Gernay T., Franssen J.-M. A formulation of the Eurocode 2 concrete model at elevated temperature that includes an explicit term for transient creep. Fire Saf. J. 2012; 51: 1–9. https://doi.org/10.1016/j.firesaf.2012.02.001
36. Wei Y., Zhang L., Au F.T.K., Li J., Tsang N.C.M. Thermal creep and relaxation of prestressing steel. Constr. Build. Mater. 2016; 128: 118–127. https://doi.org/10.1016/j.conbuildmat.2016.10.068
37. Mai V.-C., Nguyen X.-D., Nguyen C.-D. Numerical simulation for the flexural response of large-span UHPFRC prestressed composite box girder. J. Sci. Technol. Civ. Eng. 2023; 17(4): 80–94. https://doi.org/10.31814/stce.huce2023-17(4)-07
38. Wu X.-Q., Huang T., Au F.T.K., Li J. A localized fire model for predicting the surface temperature of box girder bridges subjected to tanker truck fire. Fire Technol. 2020; 56(5): 2059–2087. https://doi.org/10.1007/s10694-020-00966-2
39. Stern-Gottfried J., Rein G. Travelling fires for structural design – Part I: Literature review. Fire Saf. J. 2012; 54: 74–85. https://doi.org/10.1016/j.firesaf.2012.06.003
40. EN 1990. Eurocode - Basis of structural design. Brussels: European Committee for Standardization; 2002.
41. EN 1991-2. Eurocode 1: Actions on structures, Part 2: Traffic loads on bridges. Brussels: European Committee for Standardization; 2003.
42. Nguyen T.-N.-H., Stanton J.F., Eberhard M.O., Chapman D. The effect of temperature variations on the camber of precast, prestressed concrete girders. PCI J. 2015; 60(5): 48–63. https://doi.org/10.15554/pcij.09012015.48.63
43. Peris-Sayol G., Paya-Zaforteza I., Alos-Moya J., Hospitaler A. Analysis of the influence of geometric, modeling and environmental parameters on the fire response of steel bridges subjected to realistic fire scenarios. Comput. Struct. 2015; 158: 333–345. https://doi.org/10.1016/j.compstruc.2015.06.003
44. Timilsina S., Yazdani N., Beneberu E. Post-fire analysis and numerical modeling of a fire-damaged concrete bridge. Eng. Struct. 2021; 244: 112764. https://doi.org/10.1016/j.engstruct.2021.112764
45. Liu X., Yu C., Quan W., Chen L. Inspection, materials testing and field testing of a prestressed concrete box bridge after fire exposure. Fire Saf. J. 2019; 108: 102852. https://doi.org/10.1016/j.firesaf.2019.102852
46. Gernay T., Pei J., Tong Q., Bamonte P. Numerical analysis of the effects of fire with cooling phase on reinforced concrete members. Eng. Struct. 2023; 293: 116618. https://doi.org/10.1016/j.engstruct.2023.116618
47. Kodur V.K.R., Agrawal A. An approach for evaluating residual capacity of reinforced concrete beams exposed to fire. Eng. Struct. 2016; 110: 293–306. https://doi.org/10.1016/j.engstruct.2015.11.047